Enhanced photocatalytic activity of {1 0 1}-oriented bipyramidal TiO$_2$ agglomerates through interparticle charge transfer

Eui-Hyun Kong [a,1,2], Jonghun Lim [b,2], June Ho Lee [a], Wonyong Choi [b,*], Hyun Myung Jang [a,*]

[a] Department of Materials Science and Engineering, Division of Advanced Materials Science, Pohang University of Science and Technology (POSTECH), Pohang 790-784, Republic of Korea
[b] School of Environmental Science and Engineering, Pohang University of Science and Technology (POSTECH), Pohang 790-784, Republic of Korea

A B S T R A C T

Uniformly packed dense TiO$_2$ bipyramid agglomerates (BPA) with the dominantly exposed {1 0 1} facets were designed and synthesized by using a simple solvothermal process. From scanning electron microscopy (SEM) image, BPA consists of uniformly and densely packed nanoparticles forming secondary mesopores. BPA structure was intentionally crushed by ball-milling to obtain c-BPA, the photoactivity of which was compared with BPA. The photocatalytic activities of as-prepared BPA and c-BPA were investigated for hydrogen production and 4-chlorophenol degradation and compared with P25 as a reference TiO$_2$. The BPA showed much higher photocatalytic activities than those of c-BPA and P25 (randomly aggregated commercial TiO$_2$ nanoparticles). The marked efficiency improvement in BPA can be ascribed to the noble nanostructural features: (i) the agglomerated bipyramid (BP) units suppressing the electron-hole recombination through efficient interparticle charge transfer, (ii) the well-developed mesopores allowing the efficient diffusion of reactants and products, (iii) the highly {1 0 1}-oriented BP units that help efficient charge separation, and (iv) a good crystallinity of the BP units. These superior properties of BPA were also confirmed in their photoelectrochemical behaviors: the electrode of BPA exhibited the highest photocurrent under UV light, the slowest decay of open-circuit potential after turning off the light, and the lowest charge transfer resistance from the electrochemical impedance spectroscopic (EIS) measurement, which implies the retarded recombination of charge pairs and efficient interparticle charge transfer on BPA. The controlled agglomerated structure of the nano-sized TiO$_2$ can enhance the photocatalytic and photoelectrochemical properties through efficient interparticle charge transfer.

© 2015 Elsevier B.V. All rights reserved.

1. Introduction

Titanium dioxide (TiO$_2$) has been extensively investigated for various applications because of its practical merits as a functional material such as excellent chemical stability, nontoxicity, facile method of preparation, and low material cost [1–6]. TiO$_2$ has been the most popular photocatalyst but its performance is limited mainly because of low efficiency resulting from the rapid recombination of photogenerated charge pairs [7–9]. Many researchers have tried to solve this problem [10–15]. One of the strategies is to separate the charge pairs by the interparticle charge-transfer mechanism within the agglomerated state of TiO$_2$ [16–20]. For example, treating nanoporous thin films with titanium tetrachloride (TiCl$_4$) highly enhanced the efficiency of dye-sensitized solar cells (DSCs) by increasing the interconnection at the grain boundary among TiO$_2$ nanoparticles [16–18]. Similar behavior was observed in photocatalysis. Densely packed nanostructures enhanced the photocatalytic production of hydrogen [21–26]. Furthermore, the TiO$_2$ electrodes prepared by a sol-gel route showed higher photocurrents than those prepared by a nanoparticle-based route because a continuous TiO$_2$ network derived from the sol-gel process leads to a higher mobility of charge carriers within the TiO$_2$ electrode [27]. These results were ascribed to efficient charge separation through the interparticle charge transfer within TiO$_2$ agglomerates.

It is known that physical interconnection between nanoparticles in a TiO$_2$ agglomerate can enhance the charge separation by increasing the charge-carrier diffusion length [28]. On the other

* Corresponding authors. Tel.: +82 54 279 2283; fax: +82 54 279 8299.
  E-mail addresses: wchoi@postech.edu (W. Choi), hmjang@postech.ac.kr
(H.M. Jang).
[1] Present address: Display Materials Development Team, Electronic Materials Division, Samsung SDI, Suwon 443-803, Republic of Korea
[2] These authors contributed equally to this work.

hands, the photocatalytic activity of randomly aggregated TiO$_2$ nanoparticles can still be low because they induce numerous undesirable interfacial defects that could act as charge recombination centers [29]. Therefore, to optimize the charge-separation efficiency through the interparticle charge transfer, it is highly desirable to structurally arrange the agglomerates composed of TiO$_2$ nanoparticles in a uniformly and densely packed mode.

Several studies have reported that the hierarchically structured (HS) TiO$_2$ improves the photocatalytic activity because the active facets such as {1 0 1} and {0 0 1} can be selectively exposed [30,31]. However, the agglomeration effect on efficient interparticle charge transfer in the HS TiO$_2$ has not been studied yet. In this work, we synthesized uniformly and densely packed TiO$_2$ agglomerates consisting of ~20-nm-sized bipyramidal particles with {1 0 1}-oriented facets and studied the interparticle charge transfer in the HS TiO$_2$ agglomerate for achieving high photocatalytic and photo-electrochemical (PEC) performances.

As illustrated in Fig. 1, the present HS TiO$_2$ is featured by bipyramid agglomerate (BPA). We propose that distinct structural features of BPA may enhance the photocatalytic activity for the following reasons. Firstly, uniformly packed dense agglomerates promote an efficient charge pair separation through the interparticle charge transfer and provide accessible mesopores for the diffusion of substrates. Furthermore, the bipyramidal shape enhances the electron transfer between primary particles by increasing the contact area. Secondly, the exposed {1 0 1} facets on the bipyramidal TiO$_2$ further reduce the recombination rate because the photo-generated electrons are preferentially accumulated at the {1 0 1} facets with retarding the recombination rate [30,31]. Finally, the high crystallinity of bipyramidal particles with fewer defect sites can minimize the defect-induced recombination.
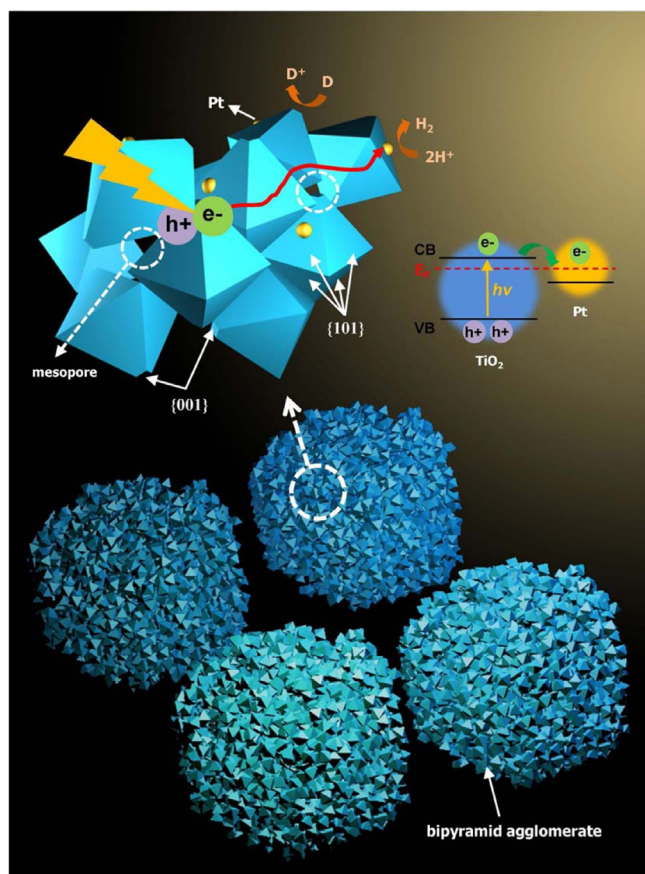

Fig. 1. Schematic illustration of the mesoporous BPA structure for facilitated charge separation.

The superior activities of {1 0 1}-oriented BPAs were demonstrated and discussed for photocatalytic and PEC performances.
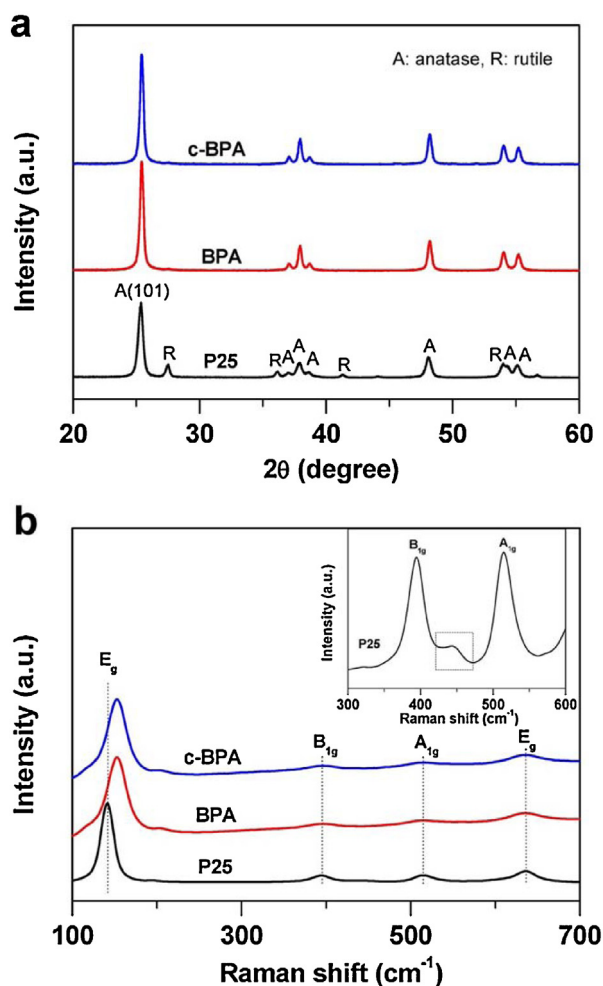
2. Experimental

2.1. Synthesis of the BPA

The BPA was synthesized using a simple solvothermal process. A precursor solution was prepared, which consisted of 2 ml titanium butoxide, 0.5 ml titanium tetrachloride (1 M in toluene), and 1 ml hydrochloric acid (37 wt%), which were dissolved in 20 ml toluene (99.5%). The resulting opaque solution was centrifuged at 3700 rpm to obtain 20 ml of transparent solution for solvothermal treatment. Then 5 ml of absolute ethanol was added as a dispersing agent of primary BP particles. Finally, the mixture was transferred to a 50-mL stainless steel autoclave, was sealed and heated for 4 h at 180 °C (heating rate: 15 °C/min) and then cooled in a box furnace. The resulting precipitates were washed with absolute ethanol. The synthesized BPA was calcined at 500 °C for 30 min to remove residual organics. The calcination process did not change the morphology and crystallography of the BPA (data not shown). The ordered BPA was intentionally disrupted by a ball-milling machine for 12 h (ball-mill speed of 30 rpm) and the resulting BPA sample with a crushed structure was labeled as c-BPA. Note that the ball-milling condition we employed (30 rpm) was very mild compared with typical ball-milling conditions (e.g., 600–720 rpm) [32,33] to minimize the ball-milling induced generation of oxygen vacancies and defects.

2.2. Characterization

X-ray diffraction (XRD; Rigaku, RINT 2000) was carried out in order to investigate the phase of each TiO$_2$ sample. Raman spectra were acquired using a Bruker Senterra Raman spectrometer. The emission line at 532 nm from a Nd:YAG Laser was focused on the sample under a microscope and the size of the aperture was 50 × 1000 μm. The power of the incident beam on the sample was 10 mW. Nitrogen sorption isotherms were obtained by using the Micrometrics Tristar 3000 system. The morphology and crystallography of the BPA were examined using a field-emission scanning electronic microscope (FE-SEM; JEOL, JSM-7401F) and a high-resolution transmission electronic microscope (HR-TEM; JEOL, JEM-2200FS) with the electron energy-loss spectroscopy (EELS) analysis, which was carried out at the National Institute for Nanomaterials Technology (NINT) in Pohang, Korea. The elemental oxidation states (Ti 2p and O 1s) of the BPA was examined by using X-ray photoelectron spectroscopy (XPS, K-alpha; Thermo VG, U.K.) with an Al monochromated X-ray source (Al Kα line: 1486.6 eV).

2.3. Photoactivity test

The photocatalytic activities of as-prepared samples were tested for hydrogen (H$_2$) production in an aqueous methanol solution and for the degradation of 4-chlorophenol (4-CP) in an aqueous solution under UV light irradiation. For the hydrogen generation experiments, the TiO$_2$ powder synthesized from the above procedure was suspended in an aqueous methanol solution ([catalyst] = 1.0 g/L, [methanol]$_0$ = 10 vol% as an electron donor, pH$_i$ 3.0). Chloroplatinic acid was then added to deposit platinum (0.1 wt%) on the surface of TiO$_2$ as a co-catalyst of hydrogen production using the photodeposition method [21]. After photodeposition of platinum for 30 min, the reactor was sealed with a rubber septum and purged with N$_2$ gas for 30 min before the UV irradiation. The photo generated H$_2$ was analyzed in the headspace of the sealed reactor by a gas chromatograph (GC, HP6890N) with a thermal conductivity detector and Ar as the carrier gas.

Fig. 2. (a) XRD patterns and (b) Raman spectra of BPA and P25. The inset in Fig. 2b presents an enlarged spectrum of P25 for the Raman shift between 300 and 600 cm^{-1}.

In the 4-CP degradation experiments, the catalyst samples were dispersed in an aqueous solution ([catalyst] = 1.0 g/L, [4-CP]$_0$ = 100 μM), and then the initial pH of the suspension was adjusted to 3.0 with HClO$_4$ solution. The solutions were continuously stirred in the dark for 30 min to achieve adsorption equilibrium. Sample aliquots were withdrawn from the reactor at constant time intervals during the irradiation, and they were filtered through a 0.45 μM PTFE syringe filter (Millipore) to remove photocatalyst particles. The degradation of 4-CP and the accompanying production of chloride were monitored using a high-performance liquid chromatograph (HPLC, Agilent 1260 Infinity) equipped with a diode array detector and a ZORBAX 300SB-C18 column (4.6 mm × 150 mm), and an ion chromatograph (IC, Dionex DX-120). A 300-W Xe-arc lamp (Oriel) was used as the light source and the irradiation was filtered through a 10-cm IR water filter and a UV-cutoff filter (λ > 320 nm) in all experiments.

Photoelectrochemical (PEC) tests were carried out using the photoelectrode on which photocatalysts were deposited. The PEC reactor contained a photoelectrode, a coiled Pt wire, and a Ag/AgCl electrode as a working, a counter and a reference electrode, respectively. These were immersed in an aqueous electrolyte of 0.2 M NaClO$_4$ (adjusted at pH 3.0) under continuous N$_2$ purging. The photoelectrodes were fabricated using the Carbowax method [23]. The coated TiO$_2$ on the FTO glass was dried for 20 min in the air and calcined at 450 °C for 1 h to burn off the organic binder. Photocurrent, electrochemical impedance spectroscopic Nyquist

plots (EIS), and open-circuit potentials (OCP) were measured using a computer-connected potentiostat (Gamry, Reference 600). The photoelectrode was biased with a potential of +0.6 $V_{Ag/AgCl}$ for photocurrent and 0 $V_{Ag/AgCl}$ for EIS measurement.

3. Results and discussion

3.1. Characterization

XRD patterns of the as-synthesized BPA, c-BPA and P25 are compared in Fig. 2a. All of the diffraction peaks of BPA are matched with the anatase phase of TiO$_2$ (JCPDS no. 21-1272). The crystalline size of primary nanoparticles in BPA was estimated from the full-width at half maximum (FWHM) of the anatase (1 0 1) peak using the Scherrer equation. The XRD-estimated size of the primary crystallites in BPA is 24 nm. A commercial TiO$_2$ sample [P25, mixture of anatase and rutile with primary particle size of 20–40 nm] that is similar to BPA in its primary particle size is compared as a reference. P25 is highly crystalline with a minor amorphous fraction (<10%) [34] and the fact that the diffraction peaks of BPA are sharper than those of anatase of P25 indicates that BPA is more crystalline than (or at least as crystalline as) P25. Additional information on the nanocrystallites can be obtained by monitoring Raman spectra. As presented in Fig. 2b, the Raman spectrum of BPA is nearly identical to that of P25 having four Raman-active modes associated with the anatase phase: E_g (145 cm^{-1}), B_{1g} (398 cm^{-1}), A_{1g} (518 cm^{-1}), and E_g (640 cm^{-1}) [35,36]. In the case of P25, however, there is a shoulder peak at ~450 cm^{-1} (See the inset of Fig. 2b), which is
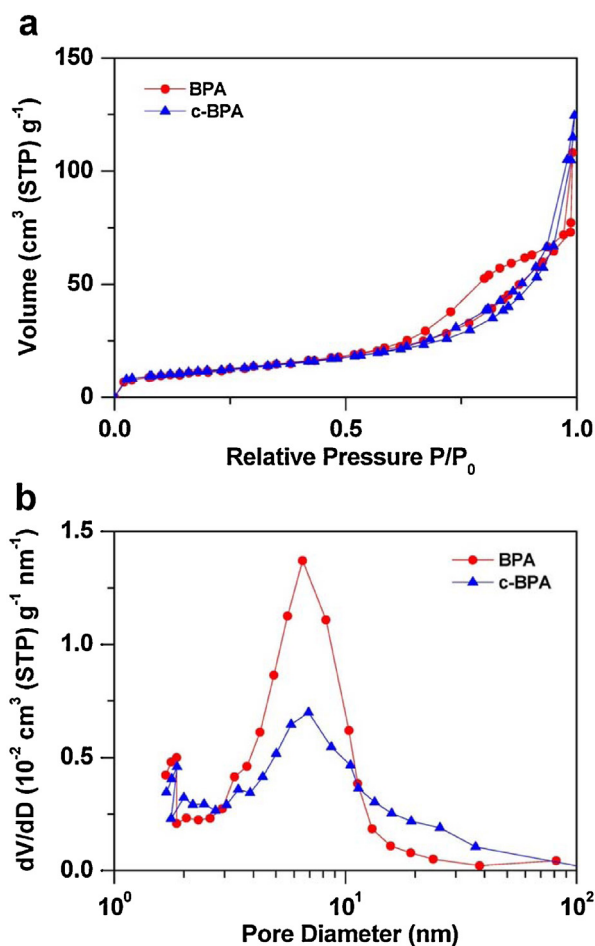
Fig. 3. (a) Nitrogen-sorption isotherms of BPA and c-BPA. (b) the corresponding pore-size distribution, estimated using the BJH model.
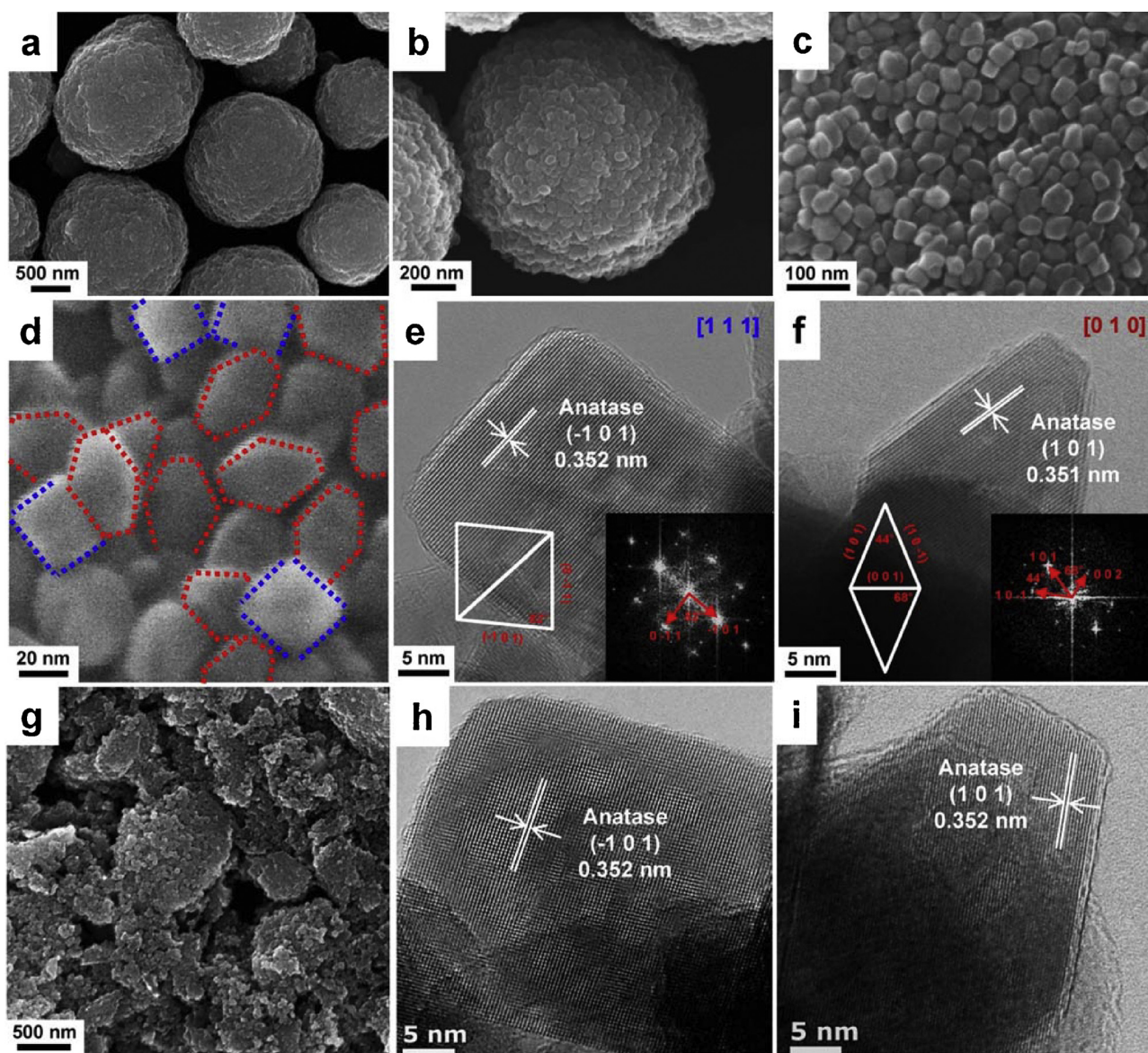
Fig. 4. SEM and TEM images of the BPA. (a–d) SEM images at various magnifications. (e, f) HRTEM images within the [111] and [010] zone axis. The inset in Fig. 4e and f are 2D models and corresponding FFT patterns. (g–i) SEM and HRTEM images of c-BPA within the [1 1 1] and [0 1 0] zone axis.

assigned to the vibrational modes of the rutile phase. As compared with P25 spectrum, the Raman peak for the E_g normal mode of BPA shows a noticeable shift to a higher wavenumber (from 145 to 155 cm^{-1}) with concomitant line broadening. The variation in the Raman active E_g mode has been attributed to the change in the vibrational amplitude and the force constant of the nearest neighbors [35,37]. The ball-milled BPA (c-BPA) does not exhibit any noticeable change in the XRD and Raman spectrum.

The surface area and the pore-size distribution were examined by adopting nitrogen-sorption analysis (Fig. 3). In order to see the effect of the agglomerate structure on the photocatalytic activities,

two distinct types of agglomerates were prepared: (i) pristine BPA and (ii) crushed BPA (c-BPA) that was processed by ball milling. Their properties are summarized in Table 1. The specific surface area was calculated by employing the Brunauer–Emmett–Teller (BET) adsorption model. For both types of samples, H1-type hysteresis [38] and type IV isotherms with a sharp capillary-condensation step were observed at high relative pressures. This suggests the presence of mesopores in both types of samples (Fig. 3a). The estimated pore size and the total pore volume are 6.53 nm and 0.1676 cm^3 g^{-1} for BPA, and 6.92 nm and 0.1937 cm^3 g^{-1} for c-BPA according to the Barrett–Joyner–Halenda (BJH) model

Table 1
Physicochemical properties of the BPA and c-BPA determined by N$_2$ sorption and XRD analysis.

Sample	BET surface area (m^2 g^{-1})	BJH cumulative pore volume (cm^3 g^{-1})	Pore size (nm)	$d_{xrd}(101)$[a] (nm)
BPA	42.0 ± 0.5	0.17	6.53	24
c-BPA	42.2 ± 0.3	0.19	6.92	24

[a] The crystallite size was calculated by applying the Scherrer equation to the FWHM of the anatase (1 0 1) peak.

a

b

c
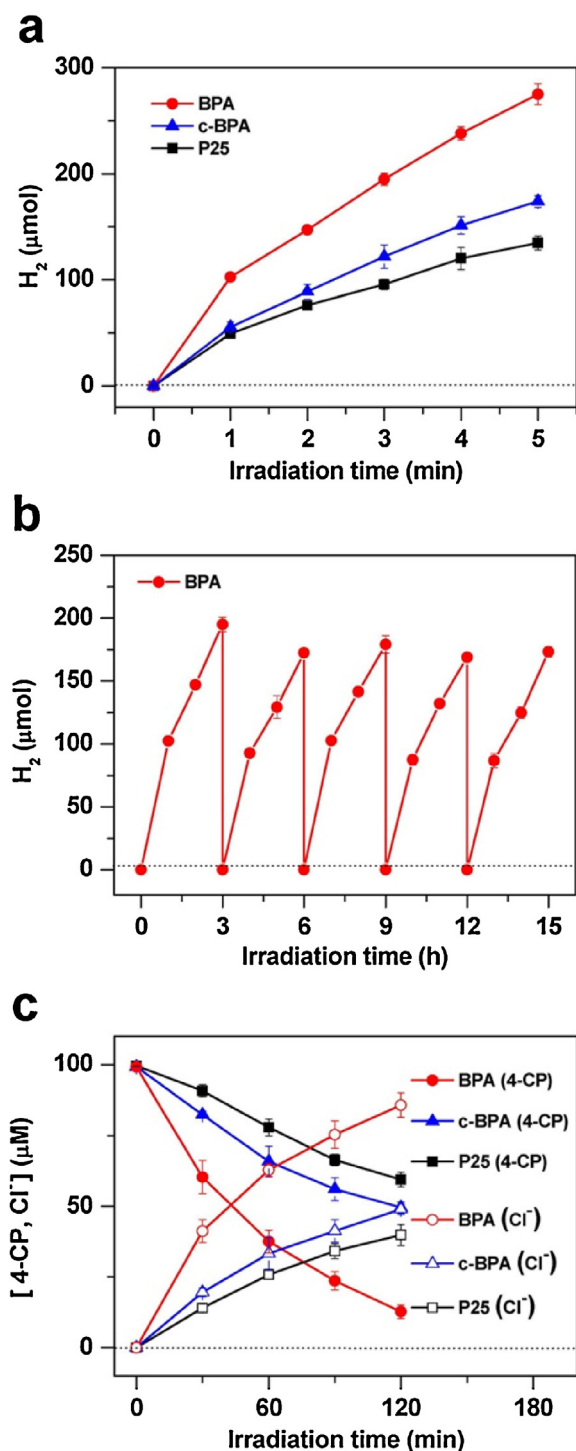
Fig. 5. (a) Time profiles of the generation of H_2 in the presence of BPA, c-BPA, and P25. (b) Repeated cycles of H_2 generation in the suspension of BPA under UV irradiation ($\lambda > 320$ nm): [TiO$_2$] = 1.0 g/L (with 0.1 wt% Pt), [CH$_3$OH]$_0$ = 10 vol%, pH 3.0, N$_2$-purged for 30 min prior to irradiation. (c) Time profiles of the degradation of 4-CP in the presence of BPA, c-BPA, and P25 under UV irradiation: [TiO$_2$] = 1.0 g/L, [4-CP]$_0$ = 100 μM, air-equilibrated.

(Table 1). After the ball-milling process, the volume of smaller mesopores (3–10 nm) decreases while that of larger mesopores (10–80 nm) increases, with a broadening in the size distribution (Fig. 3b). The specific surface area is 42.0 ± 0.5 m^2 g^{-1} for BPA and 42.2 ± 0.3 m^2 g^{-1} for c-BPA, respectively, which remains unchanged. The significant increase in the volume of large meso-

pores and the pore size after the ball-milling treatment indicates that the ordered arrangement of BP nanoparticles in the BPA structure is disrupted (at least, partly) by the ball-milling process. The fact that the ball milling did not induce any change in the XRD spectrum of BPA (See Fig. 2a) implies that the ball milling process was mild enough not to change the crystalline structure of BPA but disrupted only the aggregate structure.

Fig. 4(a–d) shows the morphological features of BPA. The field-emission scanning electron microscopy (FE-SEM) images show that BPAs of 1–1.5 μm in diameter are composed of nanobipyramids having a mean size of about 25 nm. This result is consistent with the size of ∼24 nm estimated by the Scherrer formula. High-resolution TEM (HR-TEM) images with [1 1 1] and [0 1 0] orientations were selected as major viewgraphs for the morphological analysis of nanobipyramids. As shown in Fig. 4e, the HR-TEM image with [1 1 1] orientation shows that the interplanar d-spacing is 0.352 nm which corresponds to the {−1 0 1} facet. The fast-Fourier transform (FFT) pattern shows that the angle between {0 and 11} and {−1 0 1} facets is 82°, which is consistent with the two dimensional (2D) model in the [1 1 1] zone axis (an inset of Fig. 4e). The HR-TEM image with [0 1 0] orientation is shown in Fig. 4f. The lattice spacing of 0.351 nm can be indexed to {1 0 1} facets. The corresponding FFT pattern and 2D model in the [0 1 0] zone axis show that the angles between {1 0 1} and {1 0 -1} facets and {1 0 1} and {0 0 2} facets are ∼44° and 68°, respectively (see the inset of Fig. 4f). Consequently, a nanobipyramid unit in the present TiO$_2$ agglomerate consists of eight trapezia facets based on the above data. The ordered inter-particle connection in BPA is collapsed after ball-milling process (Fig. 4g), but the shape and size of individual BP nanoparticles are not changed (Fig. 4h and i). This result is consistent with nitrogen-sorption analysis (See Fig. 3) and XRD and Raman analysis (See Fig. 2).

3.2. Photocatalytic and photoelectrochemical properties

The photocatalytic activities of BPA and c-BPA were compared along with P25 as a reference TiO$_2$ for the photocatalytic evolution of hydrogen and the degradation of 4-CP under UV irradiation. Since the ball-milling process may induce the generation of oxygen vacancies and defects in c-BPA which subsequently may reduce the photocatalytic activity, XPS spectra of Ti 2p and O 1s were compared between BPA and c-BPA samples. Any possible damages in the surface structure of TiO$_2$ should perturb the binding energies of Ti and O [39,40]. However, the XPS spectra of BPA and c-BPA did not show any noticeable difference in their binding energies (spectra not shown), which indicates that oxygen vacancy is not generated under the present mild ball-milling condition. The present mild ball-milling disrupted only the interconnection among bipyramidal (BP) units and was not energetic enough to create oxygen vacancies in the BP units. Therefore, any activity difference between BPA and c-BPA should be ascribed to the interparticle-connection character-istics because BPA and c-BPA are significantly different only in how the BP units are interconnected (inducing different mesoporous network structures) while the morphological and crystallograph-ical properties of the BP units themselves are not changed (see Figs. 2 and 4). As shown in Fig. 5a, the photocatalytic production of hydrogen with BPA was markedly higher than that with c-BPA or P25. This enhancement is due to the structural and morpholog-ical advantages of BPA, which should facilitate the separation of charge pairs through the well-connected network of the BP units. The interconnection among individual nanoparticles is important for achieving the efficient interparticle transport of charge carriers in the agglomerate of nanoparticles [21]. On the other hand, the interparticle connection in c-BPA is damaged by the ball-milling process and the network of BP units is less connected. As a result,
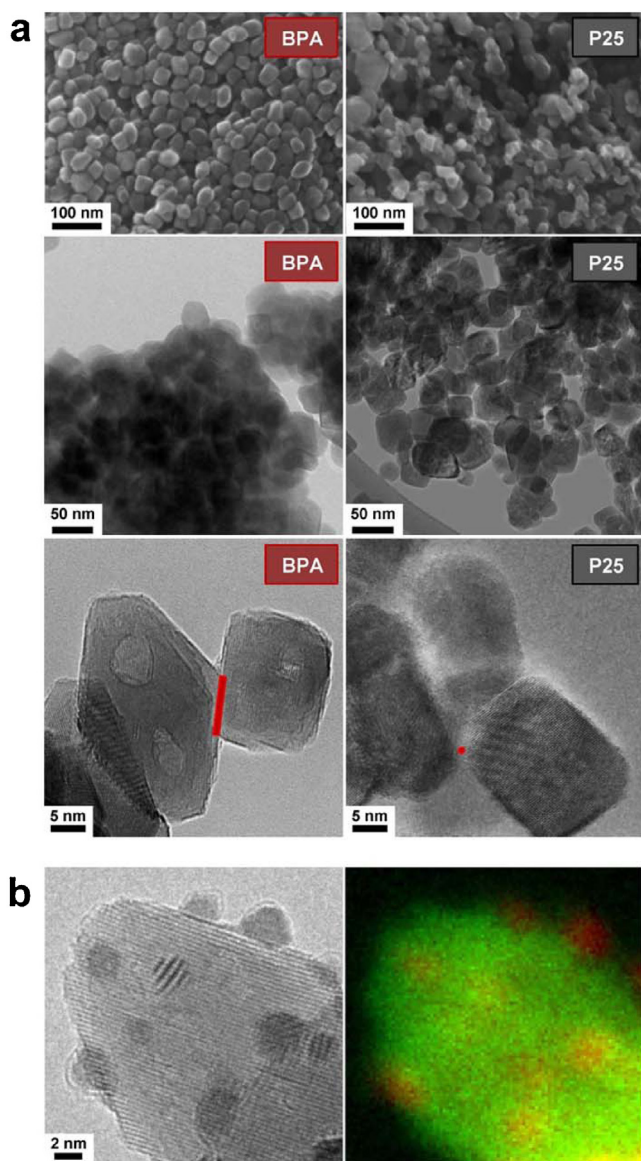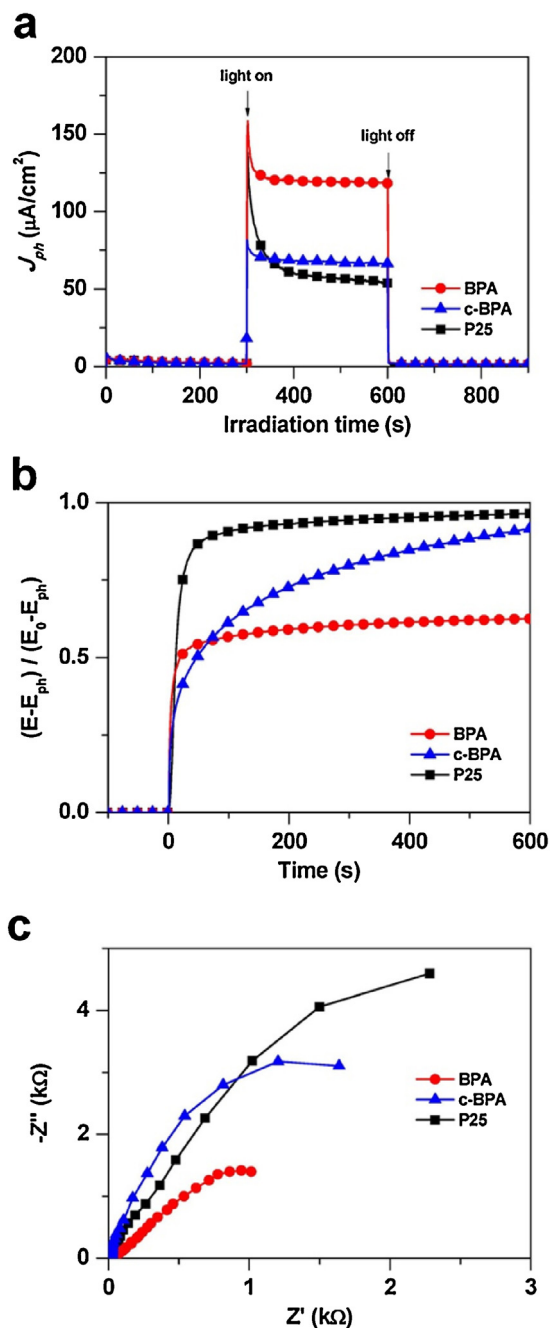
Fig. 6. (a) SEM and TEM images of BPA and P25 at different magnifications. (b) HRTEM image and EELS data of Pt on the BPA. Pt is marked with red spots, while Ti and O are marked with green spots.

Fig. 7. (a) Time profiles of photocurrent response under UV irradiation with a potential bias of +0.6 V. (b) Normalized open-circuit potential (OCP) decay curves after turning off the UV light (E_0: steady-state OCP in the dark, E_{ph}: steady-state OCP under irradiation). (c) Electrochemical impedance spectroscopic Nyquist plots under UV irradiation: [$NaClO_4$] = 0.2 M, pH 3.0, potential bias of 0 V (vs. Ag/AgCl), and continuously N_2-purged.

the efficiency of the charge-pair separation in c-BPA is expected to be reduced, which leads to a reduced photocatalytic activity.

The BP shape of the individual nanoparticle further promotes the interparticle charge transfer by increasing the contact area between the well-developed facets (see Fig. 6a): a wide contact area between the facets facilitates an efficient interparticle charge transfer and enhances the photocatalytic activity [41]. However, when nanoparticles are randomly connected, the contact area at the boundaries is limited and the charge-pair separation through the particle boundaries is somewhat hindered. Therefore, the activity of P25 that consists of randomly agglomerated TiO_2 nanoparticles is lower than that of BPA. In addition, the exposed {1 0 1} facets in anatase TiO_2 retard the recombination of photo-generated charge pairs by attracting photo-electrons, and this leads to the enhanced photocatalytic activity [29]. Lastly, enhanced light scattering by micrometer-sized spherical BPA may improve the light absorption efficiency, thereby increasing the photocatalytic activity [42]. Thus, the observed higher photocatalytic H_2 evolution in the BPA might be ascribed at least partly to the characteristics of {1 0 1}-oriented

nanometer-sized bipyramids and micrometer-sized spherical BPA particles. The Pt nanoparticles deposited on BPA as a hydrogen-evolving co-catalyst were well dispersed on the facets of the BP TiO_2 unit as shown in Fig. 6b. Incidentally, the photocatalytic activity of BPA for the hydrogen evolution was maintained during the repeated photocatalytic cycles without showing any significant deactivation (Fig. 5b).

A similar behavior was confirmed for the photocatalytic degradation (oxidation) of 4-CP. The photocatalytic oxidation efficiency that depends on the generation of reactive oxidants (e.g., hole, hydroxyl radical) is also higher with BPA than c-BPA (Fig. 5c).

Since the electron transfer should be balanced by the hole transfer to maintain the electroneutrality condition in the photocatalytic nanoparticulate system, the enhanced efficiency for the oxidative conversion (4-CP oxidation through hole transfer) is consistent with the enhanced reductive conversion (H_2 evolution through electron transfer). Although the surface area of BPA is similar to that of c-BPA, both the photocatalytic H_2 evolution and the photocatalytic oxidation of 4-CP are more efficient with BPA than c-BPA. The most plausible explanation is that the interparticle charge transfer through the dominantly exposed {1 0 1} facets is more efficient in BPA.

The charge transfer characteristics of BPA and c-BPA (loaded on the electrode) were also investigated using the PEC tests. Fig. 7a shows the photocurrent generation under UV irradiation, which is much higher with BPA than c-BPA. This is also consistent with the photocatalytic activities for hydrogen evolution and 4-CP degradation. In addition, the decay in the open circuit potential (OCP) of the BPA electrode, which was monitored immediately after turning off the UV light, is markedly slower than that of the c-BPA electrode. This implies a slower recombination rate in the BPA electrode (Fig. 7b). Such similarities between the photocatalytic activities (for H_2 evolution and 4-CP degradation) and the PEC properties clearly indicate that the structural and morphological advantages of the BPA significantly enhance the charge-separation efficiency within the agglomerate unit and reduce the recombination rate by the interparticle charge transfer through the {1 0 1} facets. To further confirm the enhanced charge transfer rate in the BPA electrode, electrochemical impedance spectroscopy (EIS) measurements were carried out. As shown in Fig. 7c, the arc size of the BPA sample is significantly smaller than that of c-BPA or P25. The smaller arc size in an EIS Nyquist plot indicates the smaller charge-transfer resistance on the electrode interface [43]. This also supports the more efficient charge transfer within the BPA electrode as compared with that of c-BPA or P25.

4. Conclusions

Hierarchically structured TiO_2 bipyramid agglomerates (BPA) with the dominantly exposed {1 0 1} facets were synthesized in ethanol as the dispersing agent. The activities and properties of BPA were compared with those of c-BPA (with partially damaged BPA structure) and P25 (commercial sample consisting of randomly agglomerated TiO_2 nanoparticles). The BPA composed of nanopyramids having a mean size of 25 nm exhibits noticeably higher photocatalytic and PEC activities in comparison to the crushed structure (c-BPA) and P25. The notable enhancement can be attributed to the unique nanostructural features of BPA**:** (i) the agglomerated bipyramid units that enable the efficient charge-pair separation through the interparticle charge transfer, (ii) the well-developed mesopores that facilitate the diffusion of substrates (reactants and products), (iii) the preferentially exposed {1 0 1} facets in the BP units that help efficient charge separation, and (iv) the good crystallinity of the BP units. We believe that the present unique approach which controls the agglomerate structure of the nano-sized building blocks can be exploited for the development of efficient photo conversion materials.

Acknowledgements

References

[1] X. Chen, S.S. Mao, Chem. Rev. 107 (2007) 2891.
[2] R. Asahi, T. Morikawa, T. Ohwaki, K. Aoki, Y. Taga, Science 293 (2001) 269.
[3] M. Grätzel, Nature 414 (2001) 338.
[4] M.R. Hoffmann, S.T. Martin, W. Choi, D.W. Bahnemann, Chem. Rev. 95 (1995) 69.
[5] Y. Zhou, Y. Liu, P. Liu, W. Zhang, M. Xing, J. Zhang, Appl. Catal. B: Environ. 170 (2015) 66.
[6] H. Park, Y. Park, W. Kim, W. Choi, J. Photochem. Photobiol. C: Photochem. Rev. 15 (2013) 1.
[7] G. Rothenberger, J. Moser, M. Grätzel, N. Serpone, D.K. Sharma, J. Am. Chem. Soc. 107 (1985) 8054.
[8] J. Lim, D. Monllor-Satoca, J.S. Jang, S. Lee, W. Choi, Appl. Catal. B: Environ. 152–153 (2014) 233.
[9] G.S. Pozan, M. Isleyen, S. Gokcen, Appl. Catal. B: Environ. 140–141 (2013) 537.
[10] N.Q. Wu, J. Wang, D. Tafen, H. Wang, J.G. Zheng, J.P. Lewis, X.G. Liu, S.S. Leonard, A. Manivannan, J. Am. Chem. Soc. 132 (2010) 6679.
[11] D. Yang, H. Liu, Z. Zheng, Y. Yuan, J.-C. Zhao, J. Am. Chem. Soc. 131 (2009) 17885.
[12] W.Y. Teoh, J.A. Scott, R. Amal, J. Phys. Chem. Lett. 3 (2012) 629.
[13] J. Lim, P. Murugan, N. Lakshminarasimhan, J.Y. Kim, J.S. Lee, S.-H. Lee, W. Choi, J. Catal. 310 (2014) 91.
[14] V. Subramanian, E.E. Wolf, P.V. Kamat, J. Am. Chem. Soc. 126 (2004) 4943.
[15] H. Tada, T. Soejima, S. Ito, H. Kobayashi, J. Am. Chem. Soc. 126 (2004) 15952.
[16] H. Yu, S. Zhang, H. Zhao, B. Xue, P. Liu, G. Will, J. Phys. Chem. C 113 (2009) 16277.
[17] H. Yu, S. Zhang, H. Zhao, H. Zhang, Phys. Chem. Chem. Phys. 12 (2010) 6625.
[18] E.-H. Kong, J. Lim, Y.-J. Chang, Y.-H. Yoon, T. Park, H.M. Jang, Adv. Energy Mater. 3 (2013) 1344.
[19] Y. Park, W. Kim, D. Monllor-Satoca, T. Tachikawa, T. Majima, W. Choi, J. Phys. Chem. Lett. 4 (2013) 189.
[20] B.C. O'Regan, J.R. Durrant, P.M. Sommeling, N.J. Bakker, J. Phys. Chem. C 14 (2007) 14001.
[21] N. Lakshminarasimhan, E. Bae, W. Choi, J. Phys. Chem. C 111 (2007) 15244.
[22] N. Lakshminarasimhan, W. Kim, W. Choi, J. Phys. Chem. C 112 (2008) 20451.
[23] N. Lakshminarasimhan, A.D. Bokare, W. Choi, J. Phys. Chem. C 116 (2012) 17531.
[24] S. Zhuo, Y. Xu, W. Zhao, J. Zhang, B. Zhang, Angew. Chem. Int. Ed 52 (2013) 8602.
[25] X. Wu, Y. Yu, Y. Liu, Y. Xu, C. Liu, B. Zhang, Angew. Chem. Int. Ed 51 (2012) 3211.
[26] Y. Yu, J. Zhang, X. Wu, W. Zhao, B. Zhang, Angew. Chem. Int. Ed 51 (2012) 897.
[27] P. Hartmann, D.-K. Lee, B.M. Smarsly, J. Janek, ACS Nano 4 (2010) 3147.
[28] A.A. Ismail, D.W. Bahanemann, J. Phys. Chem. C 115 (2011) 5784.
[29] Z. Bian, T. Tachikawa, W. Kim, W. Choi, T. Majima, J. Phys. Chem. C 116 (2012) 25444.
[30] N. Roy, Y. Sohn, D. Pradhan, ACS Nano 7 (2013) 2532.
[31] L. Ye, J. Mao, J. Liu, Z. Jiang, T. Peng, L. Zan, J. Mater. Chem. A 1 (2013) 10532.
[32] K. Saitow, T. Wakamiya, Appl. Phys. Lett. 103 (2013) 31916.
[33] S. Bégin-colin, A. Gadalla, G.L. Caër, O. Humbert, F. Thomas, O. Barres, F. Villiéras, L.F. Toma, G. Bertrand, O. Zahraa, M. Gallart, B. Hönerlage, P. Gilliot, J. Phys. Chem. C 113 (2009) 16589.
[34] B. Ohtani, O.O. Prieto-Mahaney, D. Li, R. Abe, J. Photochem. Photobiol. A: Chem. 216 (2010) 179.
[35] G. Lin, Z. Chen, C. Dong, Y. Zhao, F. Li, G.Q. Lu, J. Phys. Chem. B 110 (2006) 20823.
[36] T. Ohasak, J. Phys. Soc. Jpn 48 (1980) 1661.
[37] H.C. Choi, Y.M. Jung, S.B. Kim, Vib. Spectrosc. 37 (2005) 33.
[38] S. Lowell, J.E. Shields, Power Surface Area and Porosity, Chapman and Hall, London, UK, 1991.
[39] A.K. Rumaiz, B. Ali, A. Ceylan, M. Boggas, T. Beebe, I. Shah, Solid State Commun. 144 (2007) 334.
[40] G. Liu, H.G. Yang, X. Wang, L. Cheng, H. Lu, L. Wang, G.Q. Lu, H.-M. Cheng, J. Phys. Chem. C 113 (2009) 21784.
[41] J. Chae, M. Kang, J. Power Sources 196 (2011) 4143.
[42] D. Chen, F. Huang, Y.-B. Cheng, R.A. Caruso, Adv. Mater. 21 (2009) 2206.
[43] H. Kim, J. Kim, W. Kim, W. Choi, J. Phys. Chem. C 115 (2011) 9797.